This manuscript in post-review format was accepted for publication in Composites Science and Technology, and can be cited as follows

G. Pierreux, D. Van Hemelrijck, T.J. Massart, Automated generation of 3D orthogonal woven composites RVEs including yarn cross-section variations, Composite Science and Technology, 176, 2019, 90-102

Automated generation of 3D orthogonal woven composites RVEs including yarn cross-section variations

Gerrit Pierreux[a,b,*], Danny Van Hemelrijck[a], Thierry J.Massart[b]

[a] *Vrije Universiteit Brussel, Department of Mechanics of Materials and Constructions, Pleinlaan 2, 1050 Brussels, Belgium*
[b] *Universite Libre de Bruxelles, Building, Architecture and Town Planning Dept., Avenue Fr. Roosevelt 50, CP 194/02, 1050 Brussels, Belgium*

Abstract

This contribution presents an approach to generate unit-cell models of 3D orthogonal woven non-crimp fabric composites with the ability to incorporate cross-section variations in the weft and binder yarns. The approach starts from an initial loose-state configuration of the fiber-bundles, in which each fiber-bundle is represented by a single discretised line. The discretised lines are shaped in a step-wise generation process by geometrical operations. During the generation procedure transformed into a boundary- or inner-line configuration, respectively, to account for their cross-section variation in subsequent steps. The fiber volume fraction and fiber direction to be used subsequently in simulations are modelled on cross-sections in a post-processing step. The shape of the surface weft yarn cross-section and binder yarn cross-sections and center-line for different binder content, diameter and tensioning can be automatically accounted for. The geometrical models are then transformed into finite element models by an automated meshing procedure to investigate how the binder yarn, and cross-section variations in the surface weft and binder yarns alter the stiffness and damage initiation levels.

Keywords: 3D orthogonal woven non-crimp fabric composites, geometrical

*Corresponding author
E-mail address: gerrit.pierreux@gmail.com (G. Pierreux).

model generation, mechanical simulation, deformable binder yarn

1. Introduction

3D orthogonal woven non-crimp fabric composites consist of in-plane fiber-bundles which are straight and interwoven by a binder yarn to increase their delamination resistance [1–3]. The in-plane and out-of-plane mechanical properties of these composites have shown to be larger than 2D woven composites [4–6], showing their potential to replace the widely-adopted 2D woven composites. The properties of the 3D orthogonal woven composites can further be tailored by binder parameters as binder content, diameter, length, tension, pattern, etc. [7–12]. However, the insertion of the binder yarn distorts the reinforcement architecture of the in-plane fiber-bundles. Experimental studies remain ambiguous whether the in-plane mechanical properties are reduced, increased or left unchanged by the distortions [10, 13–15], but are clear on the fact that binder locations are acting as stress concentration regions that cause early damage initiation [5, 7, 16]. Unit-cell models have therefore shown to be a valuable approach to help understanding experimental observations or to even predict the mechanical behaviour of 3D woven composites. [17–19]. The main geometrical features of the reinforcement architecture therefore need to be characterised and included in the models.

Centerline deflection and cross-section variations in the surface weft yarn and the binder yarn are the main geometrical characteristics which are present in 3D orthogonal woven composites that will be considered in this work. Their shape and size further depend on the binder parameters and manufacturing conditions [20–22]. The binder content affects the cross-section variations and corresponding fiber waviness in the surface weft yarn [7]. The binder yarn tensioning can cause deflections of the surface weft yarn centerlines, and corresponding distortions in the underlying warp yarns, and generates higher compacted stages of the binder yarn itself. The cross-section in the top segment of the binder yarn

(Z-crown) are hereby more compacted than the cross-sections in the through-the-thickness segment [22, 23]. Transverse compaction can further cause the sinking of Z-crown into the surface weft yarn [24, 25] and the flattening and widening of the warp and weft yarns. Asymmetrical shapes of the binder yarn [26], crimping of the through-thickness segment of the binder yarn [27, 28] and fiber-breakage during 3D weaving [29] can also arise.

Analytical modelling approaches have been adopted in [21, 30, 31] to include the main features in geometrical models. In earlier models, the warp and weft yarns are considered straight with constant cross-sections along their centerline. In more advanced models, centerline deflections and cross-section shape variations in the warp, weft and binder yarn have been accounted for [30]. Energy-based approaches could then be used on analytical models to predict the centerline position and the cross-section dimensions of the fiber-bundles for different in-plane and compaction loading stages [32–34], while elliptical-shaped cross-sections of the fiber-bundles were assumed.

Image-based approaches were adopted in [25, 26] to generate realistic geometrical models of 3D woven composites. To this end, the images of micro-CT scans were transformed into a voxel-based mesh representation [26] or into a tetrahedral mesh representation [25].

A digital element approach was adopted in [35–45] to generate 3D woven composite models, in which the shape of centerlines and cross-sections of the fiber-bundles are obtained computationally during a finite element simulation. Initially, a loose-state configuration of the binder yarn inbetween the warp and weft yarn is assumed. The fiber-bundles can then be transformed into a single- or a multi-line configuration of frictionless connected bar or rod elements. A thermal contraction is further applied on the binder yarn, followed by a global compaction on the unit-cell model, while contact elements account for fiber-bundle interaction to generate the geometrical model. Stig adopted also a finite

element framework to generate 3D woven composite models [46, 47]. The fiber-bundles are then transformed into a shell element representation with the shell elements being positioned along their contour resulting in a tube structure. A hydrodynamic pressure is further applied on the tube representation to gradually inflate the fiber-bundles until a desired fiber-bundle volume fraction, while contact elements accounting for fiber-bundle interactions at intepenetrating locations causes deformable cross-section shape variations of the fiber-bundles.

Recently, a geometry-based framework to generate 3D woven unit-cell models was used in [48, 49]. The fiber-bundles are represented by a single discretised line and a constant cross-section. The discretised lines are shaped by straightening operations until an equilibrium between fiber-bundle movements is obtained, with a contact treatment accounting for the line interactions. This geometry-based framework was adopted later on to generate Z-pinned and stitched laminate unit-cell models [50, 51]. Potential resin-rich regions and out-of-plane undulations in the laminae are hereby represented by initial straight discretised lines while the pin and stitching yarn are represented initially by a single discretised line. The discretised lines are shaped in step-wise manner by geometrical operations while the contact treatment accounts for line interactions. The initial single-line configuration of the stitching yarn could hereby be transformed in a generation step into a multi-line configuration to account in subsequent steps for its cross-section variations.

Here, 3D orthogonal woven non-crimp fabric composites unit-cell models which include cross-sections variations in the weft and binder yarns are generated by an adopted geometry-based framework. The approach starts from an initial model on which geometrical operations are applied to introduce in a step-wise manner geometrical features. The cross-section variations for the weft and binder yarns are accounted for by a boundary- and inner-line configuration, respectively. Experimental data on the shape of yarns will be used to set the initial model parameters and geometrical operations parameters. The shape of

the generated geometrical features is obtained automatically. The originality of the approach is two-fold: firstly, the approach reduces the amount of experimental input data needed to generate unit-cell models compared to analytical modelling approaches. Secondly, the approach presents an unified approach that can be used to generate different morphology of 3D reinforced composites (pinned, stitched, 3D orthogonal woven) with the same tool (as adopted in [51]). The geometrical models are then transformed into finite element to investigate how the 3D weaving and the cross-section variations in the weft and binder yarn affect the stiffness and potential damage initiation.

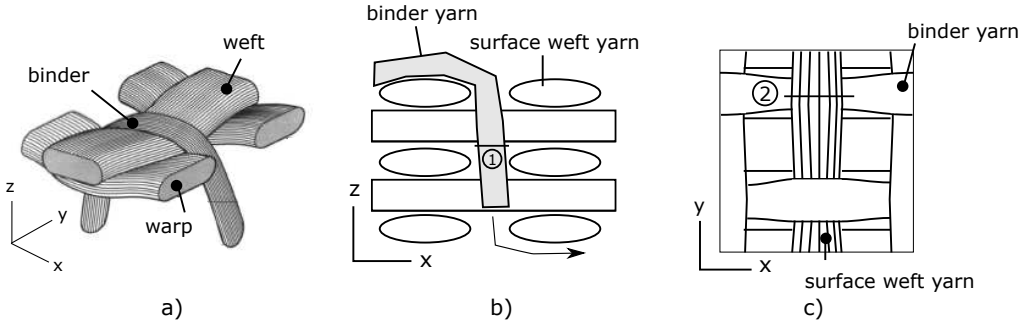

Figure 1: 3D orthogonal woven non-crimp fabric composite: (a) 3D view (taken from [52]), (b) side view, (c) top view.

2. Geometric model generation

Unit-cell models of a 3D orthogonal woven non-cimp fabric composites are generated. The warp yarns are assumed to remain straight with constant cross-section while the weft yarns are assumed to remain straight but with cross-section that are allowed to deform upon binder insertion. The binder yarn is allowed to vary in centerline and cross-section shapes, corresponding to different binder yarn tensioning states. Fiber-breakage, asymmetrically-shaped binder yarn profile, crimping of the through-thickness segment of the binder yarn are not considered in the modelling.

To generate realistic unit-cell models, experimental data will be used to set the initial model parameters and the parameters of the geometrical operations (see subsequent subsections). Hereby, the initial model parameters will implicitly take into account the global effect of transverse compaction and binder yarn tensioning on the in-plane fiber-bundle geometries, while the effect of transverse compaction on the cross-section shapes of the binder yarn is not considered in this work. The parameters of the geometrical operations can be set by combining a desired size of geometrical feature with the figures that are obtained from a parametric study that will be provided in section 4. The shape of the geometrical features will be obtained automatically. The model generation approach can therefore be seen as a tool to analyse the effect of geometrical features and/or to construct physical-comparable models when experimental data is available in an efficient way.

2.1. Initial model

Each yarn is initially represented by a single line and a constant cross-section (see Fig. 2). The lines representing the warp and weft yarns are straight, while the line representing a binder yarn is S-shaped, mimicking a loose state configuration of the binder yarn around the warp and weft yarns. Elliptical, power ellipse and rectangular cross-sections are considered for the binder yarn, the inner weft and warp yarns, and the surface weft yarns, respectively. The rectangular cross-section shape of the surface weft yarns will subsequently be shaped during the generation process. The lines are further discretised in line segments with a length e_{line} of $100\mu m$.

The (constant) cross-section shape and dimensions for the fiber-bundles can be extracted from experimental data as follows: (i) for each in-plane warp and inner weft yarn, the cross-section is taken as an average of the cross-sections along their centerline, (ii) for a surface weft yarn, the width and the height of the rectangular-assumed initial shaped cross-sections are taken as the width of the inner weft yarns and the height of surface weft yarn cross-sections outside

the distorted zone (see location 2 in Fig. 1c), respectively, (iii) for the binder yarn, the cross-section is taken as the cross-section in the middle of the through-the-thickness segment of the binder yarn (see location 1 in Fig. 1b).

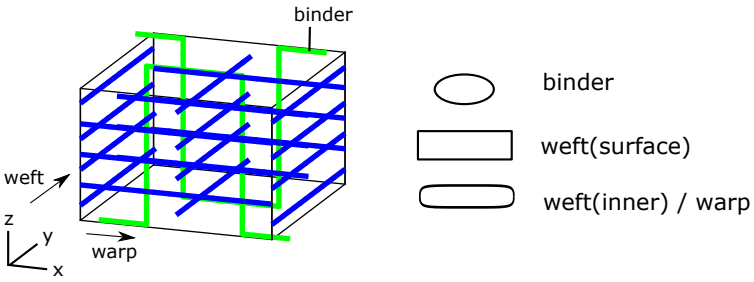

Figure 2: Initial model with a fiber-bundle represented by a single line and constant cross-section.

2.2. Boundary-line and inner-line configuration for fiber-bundles

A boundary-line and an inner-line configuration are used for the weft and binder yarns, respectively, to account for their cross-section variations.

1. In a boundary-line configuration, the lines are positioned near the boundaries of the fiber-bundles (see Fig. 3a). The cross-sections of an initial single-line configuration are discretised using circles. The circles can be positioned uniformly along the cross-section boundary or can be positioned dependent on the local curvature of the cross-section boundary. A radius is assigned to the circles to facilitate contact treatment. However it can be chosen to vanish, as the boundary-lines do not represent anything physically and contact treatment, between the boundary-lines and the binder, can still be resolved by the binder yarn radius itself. The number of circles defines the geometrical accuracy of the cross-section shape variations in a post-processing at the expense of a higher computational cost.
2. In an inner-line configuration, lines are positioned in the interior of a fiber-bundle (as introduced in the work [51]). The cross-sections of the initial single-line configurations are discretised in circles positioned inside

the cross-section. The circles can be defined as the nodes of a 2D mesh generated on the cross-section. The radius of circles is related to the number of circles and the initial fiber volume fraction in the binder yarn. The number of circles is assessed by means of a convergence study on a tensioned binder yarn.

A boundary-line configuration can be favored to account accurately for local cross-section shape distortions at a reduced computation cost, but the center-line of the corresponding fiber-bundles should remain straight. An inner-line configuration can then be used to account for cross-section variations in fibers-bundles with centerlines that should not remain straight, but at the expense of a reduced control over the final cross-section. Note that a special attention needs to be given for a boundary-line configuration to not result in a shape that exceeds locally the maximum fiber volume fraction, while this conditions is automatically satisfied for an inner-line configuration.

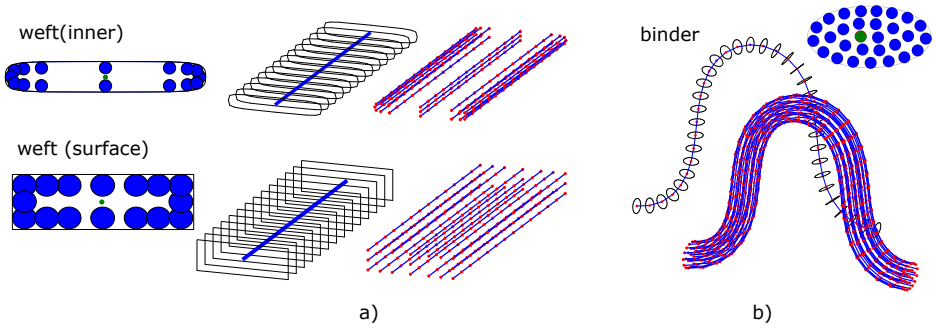

Figure 3: Different line configurations for a fiber-bundle: (a) a boundary-line configuration for the weft yarns, (b) an inner-line configuration for the binder yarn.

2.3. Geometrical tools

The geometrical operations are applied on the discretised lines in a step-wise manner, with a straightening operation as the only operation adopted in the presented generation process. Each step intends to introduce a geometrical feature in the model or to transform the single-line configuration of the weft

or binder yarns into a multi-line configuration (see Table 1). The number of straightening operation that should ideally be applied in a certain step should be deduced from a desired size of geometrical features and the graphs which will be presented in section 4. A contact parameter q (see section 2.3.2), which regulates the relative movement between two lines upon contact, will be used to constrain certain types of lines during a generation step. Boundary conditions can be enforced on the bottom and top of the surface weft yarns to keep them straight. The generation stages are illustrated in Fig. 4 and described in the sequel, followed by a short description of the adopted geometrical operations.

Step 1, the weft yarns are transformed in a boundary-line configuration.

Step 2, the binder lines (representing a single line configuration of the binders at this stage) are first made conform with the shape of the surface weft yarns by an applied straightening operation, in order to have a binder yarn shape independent of its initial position (the weft lines are constrained during this operation).

Step 3, the binder lines are then further subjected to the same straightening operation, but whereby the weft lines were unconstrained this time. The center-line of the binder yarn, and simultaneously the cross-sections of the surface weft yarns underneath the binder yarn, can hereby be shaped to account for different binder yarn tensioning levels.

Step 4, the boundary-lines of the weft yarns are straightened to smooth their locally distorted shape near the binder yarn (the binder lines are hereby constrained during this operation).

Step 5, the binder yarn is transformed into a multi-line configuration.

Step 6, the binder-lines are tensioned by the straightening operations to generate cross-section variations of the binder yarn which can correspond to different binder-yarn tensioning (the weft lines are hereby constrained).

Step 7, the bottom and the top of the unit-cell box, which surrounded initially only the warp and weft yarns, can be adjusted to generate models wherein the binder yarn is fully embedded in the matrix.

Step 8, the local fiber volume fraction and fiber direction in each fiber-bundle are obtained in a post-processing step.

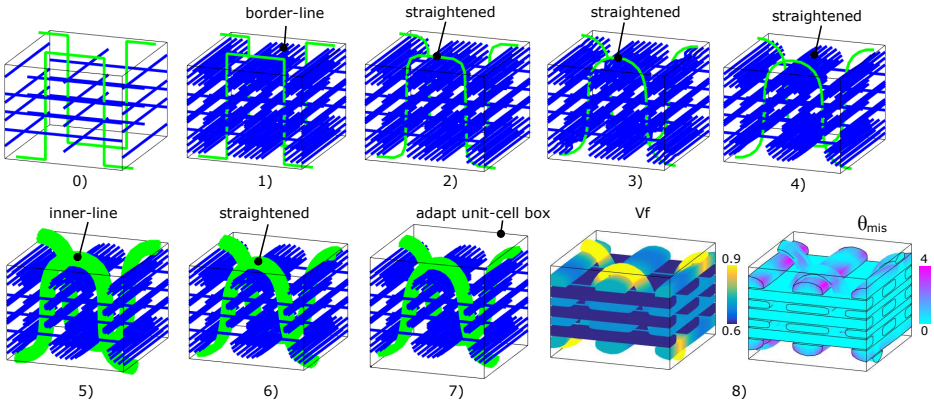

Figure 4: Step-wise generation process: (0) initial model, (1) transformation weft into boundary-line configuration, (2) binder straightening, (3) binder straightening, (4) weft straightening, (5) transformation binder into multi-line configuration, (6) binder straightening, (7) adjusting bottom and top surface of unit-cell box, (8) calculating the fiber volume fraction V_f and fiber misalignment θ_{mis} in post-processing step with θ_{mis} corrected from the local normal orientation for each fiber-bundle.

2.3.1. Straightening operation

The straightening operation repositions the nodes of a line according to [48]:

$$\vec{x}_i = (1/2).(\vec{x}_{i-1} + \vec{x}_{i+1}) \tag{1}$$

To further account for the potential effect of neighbouring unit-cells on the shape of the lines, the lines which are straightened are extended first, before straightening, at their sides by their replicates, where, after straightening, the extended parts are removed (Fig. 5). The shape of the lines is hereby controlled by the number of applied straightening operations (s) during the generation step .

2.3.2. Contact treatment

Due to the straightening operation, interpenetrations between cross-sections associated to lines may occur. A node P of a line i (see Fig. 6) which interpen-

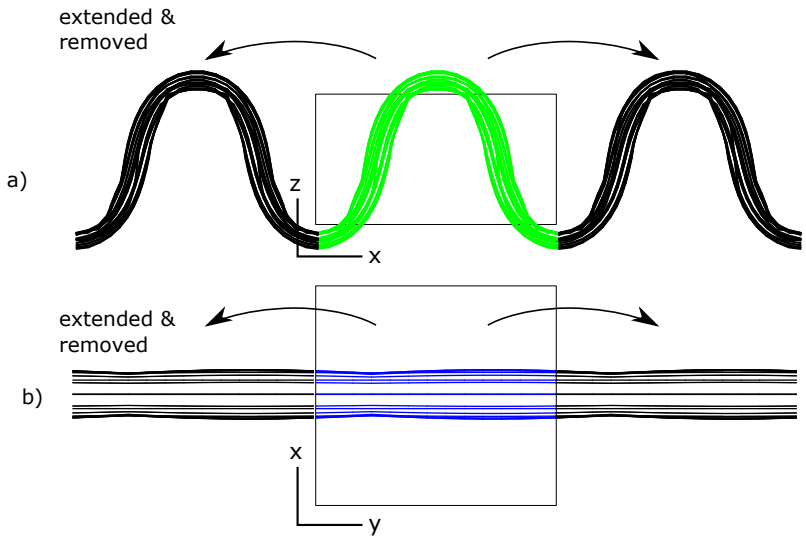

Figure 5: Extending the lines prior to straightening for: (a) binder yarn and (b) weft yarns.

etrates a line j is to be moved along its normal $\vec{D}_P$ on the line j to suppress the interpenetration [48, 50]. The movement $\vec{x}_P$ of the node P can further be regulated by a parameter q :

$$\vec{x}_P = q.d_{int}.\vec{D}_P \tag{2}$$

where d_{int} is the interpenetration distance. The parameter q controls the interaction between the lines. There is a q value for each interaction, i.e. for each pair of lines (q is not attached to a single line). The q value can be set differently dependent on the type of interacting lines interacting (see Table 1) in certain generation steps. A 0-value is considered for interacting weft yarn lines, which allows the weft yarn lines to remain interpenetrated. A 0.50-value is considered for interacting binder-lines as such to mimic a symmetrical contact between these lines. A parameter q_{bw} is used to control the interaction between a weft-line and a binder-line and can be set to 0 or 1 to constrain (i.e. keep fixed) the position of either the weft lines or the binder lines upon their interaction, respectively, in the different steps mentioned above. The controlled interaction between the weft-line and the binder-line allows further the step-wise controlled

introduction of geometrical features, feature-by-feature, which is considered as a key advantage feature of the approach.

	binder	weft
binder	0.50	q_{bw}
weft	(1-q_{bw})	0

Table 1: Different contact parameter q dependent on the type of interacting lines.

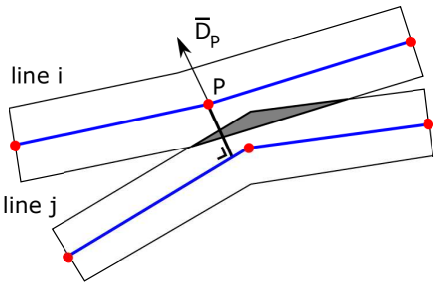

Figure 6: Contact treatment.

2.4. Fiber volume fraction and fiber direction

A constant fiber volume fraction and linear fiber direction distributions are modelled on the cross-section of the fiber-bundles. The cross-sections are obtained by intersecting the multi-line configuration perpendicular to a local tangent to the centerline, whereby the centerline of the boundary-line configuration is a straight line positioned in the center of the initial cross-section and the centerline of the inner-line configurations is the line connecting the center point in the initial inner-line configuration. An example of generated cross-section for a binder yarn and a surface weft yarns are illustrated in Fig.7.

The fiber volume fraction $V_f(s)$ in a cross-section at the position along the yarn (and that is assumed uniform in a given cross-section) is obtained by:

$$V_{f,deform}(s) = \frac{A_{init}}{A_{deform}(s)}.V_{f,init} \tag{3}$$

where A_{deform} is the deformed cross-section area and $V_{f,init}$ is the initial fiber volume fraction in the yarn. A_{init} represents the initial cross-section area, except for the surface weft yarns which have an enlarged cross-section due to their rectangular shape. For these yarns, the initial cross-section area of the inner weft yarns is considered. An example of obtained fiber volume fraction distribution along the yarn for the binder and surface weft yarns is illustrated in Fig. 7b.

The linear fiber direction in each cross-section can be obtained from a linear interpolations between the local tangent of the lines which are positioned near the boundary of the cross-sections. The fiber misalignment θ_{mis}, as often used to visualize the local fiber direction inside yarns, is defined in each cross-section as the angle between the local fiber direction and the local tangent of the centerline of the yarn at that cross-section. An example of the fiber misalignment distribution obtained for the binder and surface weft yarns is illustrated in Fig. 7c.

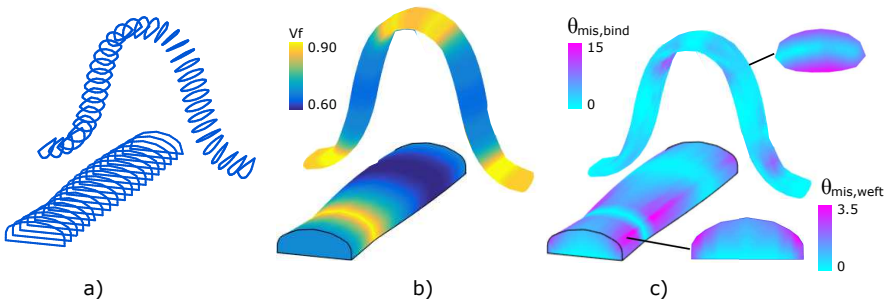

Figure 7: Surface weft and binder yarn after post-processing: (a) generated cross-sections, (b) fiber volume fraction distribution (V_f), (c) fiber misalignment distribution (θ_{mis}).

2.5. Interpenetration suppression and gap generation

Interpenetrations can take place between the binder and weft yarns. These interpenetrations are in a first instance partially avoided by increasing and decreasing the cross-section dimensions of the binder yarn before and after model

generation respectively. Residual interpenetration between the binder and weft yarns are suppressed by moving points of a triangulated binder yarn surface that interpenterates the weft yarns along a local normal on the binder yarn surface (see Fig. 8), while a gap can be inserted simultaneously. The fiber volume fraction in each cross-section of the binder yarn is afterwards adapted to account for the (small) cross-section area changes.

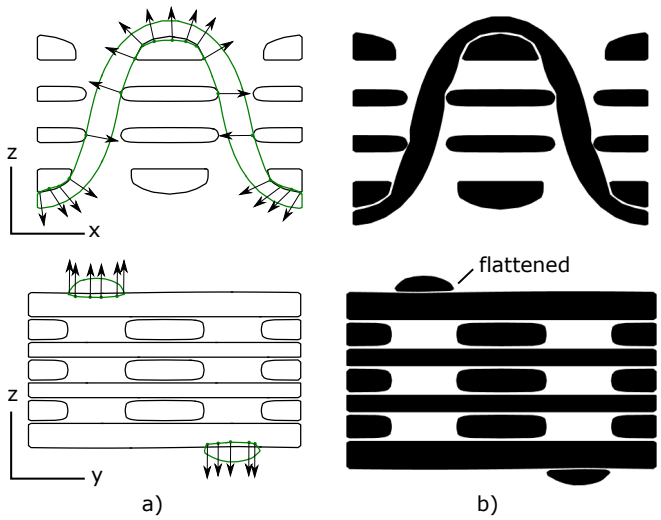

Figure 8: Interpenetration suppression and gap insertion methodology: (a) before post-processsing, (b) after post-processing.

3. Reference material geometry

The geometry corresponding to a physical material sample taken from the contribution [53] is adopted in this work for the geometrical model generation.

This geometry was obtained in [53] based on CT scanning, and represents a 3D orthogonal woven composite. Both a micro-CT scan and an analytical model were used in [53] for simulations. For the analytical model, the following assumptions were made:

1. A power-ellipse shaped cross-section is used for the in-plane warp and inner weft yarns which is constant along the yarn centerline.
2. A semi-lenticular shaped cross-section is considered for the surface weft yarns which is constant along the yarn centerline.
3. A power-ellipse shaped cross-section for the binder yarn, with a width and a height that gradually increases and decreases, respectively, from the middle of the through-the-thickness segment to the top segment of the binder yarn.
4. A binder yarn centerline position, constructed via B-spline, that is implemented manually to be conform with the surface weft yarns shape.

Full details and illustrations of this reference geometry are provided in reference [53]. Similar cross-section shapes and dimensions were adopted in this work for the initial model construction (see Table 3). The lenticular shape of the surface weft yarn, the centerline position of the binder yarn and the cross-section height reduction in the top-segment of the binder yarn are used in the qualitative comparison of the generated models.

4. Generated geometrical features

First, geometrical models are generated to illustrate the potential of the approach to generate automatically different shapes of geometrical features that can correspond to different binder parameters. The initial model parameters are set according to the information provided in Section 3. The parameters of the geometrical operations are varied to study their influence on the generated features. The generated shapes are qualitatively compared with the reference geometry from Section 3. The illustrations can further be used to set the values of the geometrical operation parameters in order to obtained the desired sizes for each introduced geometrical feature. In a second phase, models for different binder content are generated to illustrate the generality of the approach. For both cases, the generation strategy and parameters adopted to generate the geometrical models are presented in Table 2 and Table 3, respectively.

step	operations	id line	q_{bw}	parameter	geometrical feature
1	boundary-line configuration	weft	-	-	-
2	straightening	binder	0	-	-
3	straightening	binder	q_1	s_1	centerline of binder yarn
4	straightening	weft	1	s_2	cross-sections of weft yarn
5	inner-line configuration	binder	0	c	-
6	straightening	binder	0	s_3	binder yarn tensioning
7	adjusting box	-	-	(no-yes)	matrix

Table 2: A description of the step-wise generation process in terms of geometrical operations, corresponding parameters (s_i are numbers of straightening operations, c is the number of lines used in an inner line configuration), the types of lines on which the geometrical operation are applied in each step, the contact parameter in each step and the geometrical feature for which experimental observations can be used to set the corresponding parameter.

initial model	yarn	shape	a(μm)	b(μm)	n	V_f^{init}	$A_{init}(\mu m^2)$
	weft surface	rectangle	525	130	-	0.700	156.50
	weft inner	super ellipse	525	80	5	0.700	156.50
	warp	super ellipse	430	110	5	0.700	176.25
	binder	ellipse	280	150	-	0.600	136.00
generation	$s_1 = 7$, $s_2 = 50$, $c = 15$, $s_3 = 5$, adjust box = no						

Table 3: Initial model and generation parameters for the 3D woven model.

4.1. Centerline of the binder yarn and corresponding cross-section of the surface weft yarn underneath the binder yarn

The centerline of the binder yarn can be shaped in generation step 3 by the parameters s_1 and q_{bw}, while the cross-section of the surface weft yarns are shaped simultaneously (due to the contact treatment). Shapes for different values of s_1 and q_{bw} are illustrated in Fig. 9a and Fig. 9b respectively. A wide range of possible positions of the centerline of the binder yarn can be generated while the shape of cross-sections of the surface weft yarn tends towards a lenticular shape. Such a lenticular shape is often used in analytical modelling approaches [26] as well as in the reference material geometry [53] considered in this work (see Section 3).

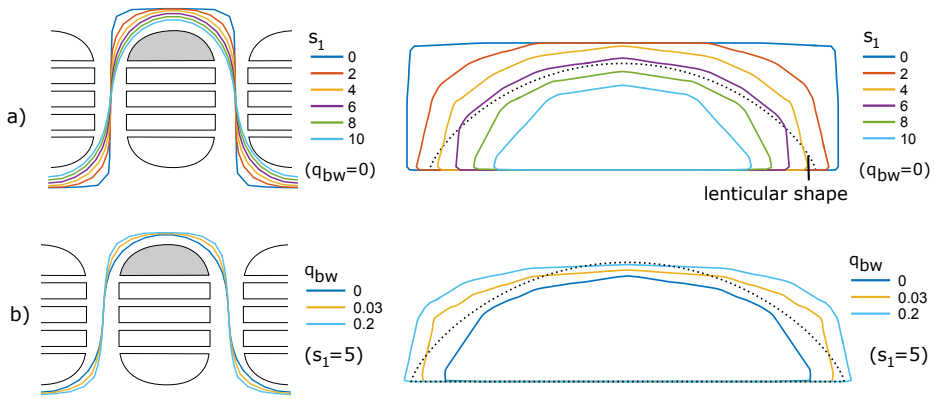

Figure 9: Different shapes of the binder yarn centerline and surface weft yarn cross-section underneath the binder yarn for varying: (a) straightening parameter s and (b) contact parameter q_{wb}.

4.2. Cross-section variations in the surface weft yarns

The cross-sections variations in the surface weft yarns are controlled in generation step 4 by the parameter s_3. The shape of the surface weft yarns for different values of s_3 are illustrated in Fig. 10 by means of the fiber volume fraction and fiber misalignment distributions in the surface weft yarns. The parameter s_3 can then be set by comparing for example the maximum in-plane fiber misalignment in the model with the maximum in-plane fiber misalignment in experimental observations, which will dependent on the binder content and tensioning. A fully straight configuration of the surface weft yarns can be obtained in the limit ($s_2 = +100$). The constant cross-section configuration of the surface weft yarn corresponds to the reference material geometry [53] considered in this work. In practice, for smaller binder contents, slight waviness in the surface weft yarn cross-section can be present, which then can seamlessly be introduced by slightly reducing s_2 towards a desired fiber-waviness in the surface weft yarn.

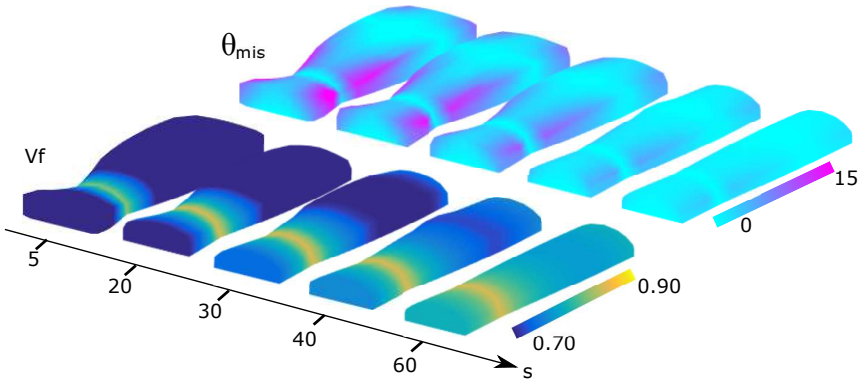

Figure 10: Cross-section variations in the surface weft yarn for varying straightening parameter s_2, illustrated by the fiber volume fraction V_f and fiber misalignment θ_{mis} distribution.

4.3. Cross-section variations in the binder yarn

4.3.1. Convergence study on the number of lines

The number of lines (c) present in the multi-line configuration of the binder yarn is set (in generation step 5) to have converged tensioned binder yarn geometries. The effect of the number of lines of the inner-line configuration on the cross-section shapes and fiber volume fraction distributions in the binder yarn is illustrated in Fig. 11. A convergence in cross-sections shapes and corresponding fiber volume fraction distributions is taking place and this (already) for a number of lines equal to 15 which will further be used in the generation process (see Table 2).

4.3.2. Mimicking different binder yarn tensioning

Cross-section shape variations in the binder yarn for different binder yarn tensioning states can be regulated in generation step 6 by means of parameter s_3. The cross-section shapes and corresponding fiber volume fraction distributions for different values of s_3 are illustrated in Fig. 12. The cross-section shapes in the top segment are flattened first and then widened for increasing values of s_3, while the cross-section shapes in the middle of the through-the-thickness segments of the binder yarn are barely changed. A binder yarn configuration which is conform with a physical observation can then be generated by setting

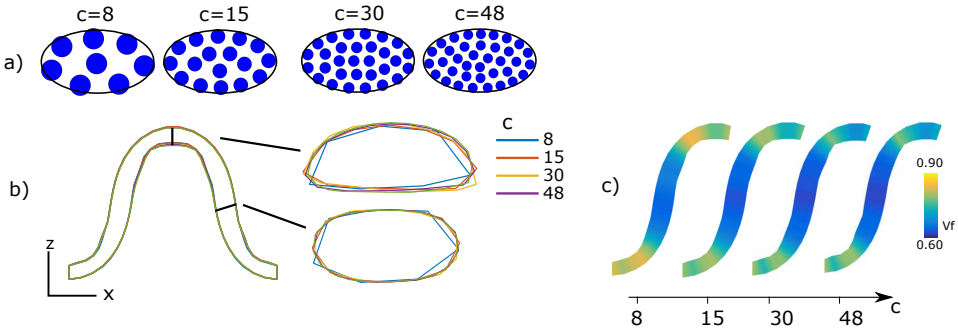

Figure 11: Convergence study on the number of lines c for a tensioned binder yarn: (a) different cross-section discretisations, (b) cross-section shape variations, (c) fiber volume fraction V_f distribution.

first the initial cross-sections of the binder yarn to a cross-section located in the middle of the through-the-thickness segment of the physical binder yarn, whereafter parameter s_3 should be set by comparing for example the thickness of the cross-section at top segment. Typical cross-section thikness reductions in the top segment of the binder yarn for different binder yarn tension-levels lie between 0.30 and 0.70 [7, 20, 21, 30, 34].

The modelling approach could further generate realistic models based on the loom set-up. The tensioning levels in the weft and binder yarns should be related via experimental images with the size of the geometrical features. The size of the geometrical features could then be used to obtain the different generation parameters using the graphs represented in Section 4. The value of the generation parameters could then be set automatically at the start of the generation process to create physically related models.

4.4. Geometrical models for different binder content

Models for different binder contents are now generated and illustrated in Fig. 13. The binder yarn content is varied from 0.5% to 4% by changing the unit-cell dimensions while the binder diameter is kept constant. It can be seen that the approach accounts automatically for different shapes of the surface weft yarns

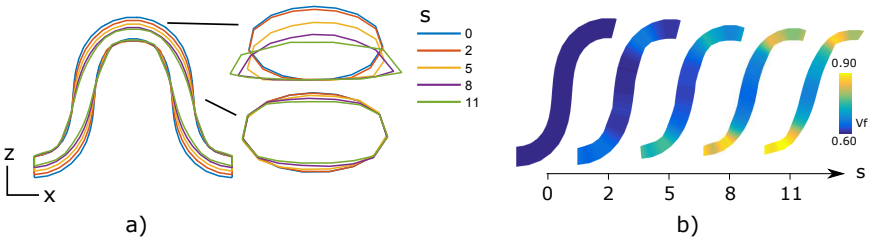

Figure 12: Shapes of a tensioned binder yarn for varying parameter s_3: (a) cross-section shapes of the binder yarn, (b) fiber volume fraction V_f distribution in the binder yarn.

corresponding to the different binder content.

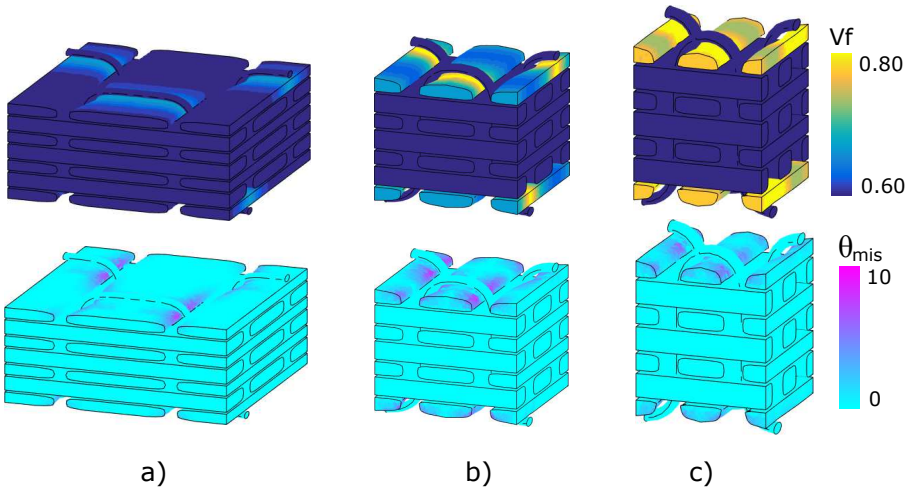

Figure 13: 3D woven models for different binder content (represented by their fiber volume fraction V_f and fiber misalignment θ_{mis} distribution): (a) binder content of 0.50%, (b) binder content of 2%, (c) binder content of 4%.

5. Mechanical simulations

Upon availability of the geometry generated by the proposed procedure, the geometrical models are transformed into finite element models using the meshing software GMSH. Periodic boundary conditions are applied on the in-plane unit-cell surfaces while the bottom and top of the unit-cell are left free. Carbon fibers and epoxy matrix are considered as constituent materials with

mechanical properties presented in Table 4. The mechanical properties of the fiber-reinforced region are obtained, in function of the local fiber volume fraction, by means of the Chamis-formulae [54]. A global strain of 0.50% is applied on the unit-cell models in the warp-, weft- and bias(45°)-direction, a straining level that has been shown experimentally to cause early damage initiation in 3D woven composites [5, 16].

The stiffness of the unit-cell model is then computed and normalised by the stiffness of an equivalent non 3D-woven composites (described in Section 5.1). The local stress levels are evaluated based on their potential to initiate damage. Transverse cracking (via f_{22}) and shear cracking (via f_{12}) in the fiber-reinforced regions, debonding at the interface between the fiber-reinforced regions and the matrix (via f_{int}) and matrix cracking (via f_m), are considered as damage initiation mechanisms in fiber-reinforced composites [24, 55–57]. Each damage initiation mechanisms is evaluated by a local damage initiation indicator f_{ij} defined by:

$$f_{22} = \frac{\sigma_{22}}{X_{22}(V_f)}, \quad f_{12} = \frac{\sigma_{12}}{X_{12}(V_f)}, \quad f_m = \frac{\sigma_p}{X_t} \quad (\geq 1)$$

where σ_p is the maximum tensile principal stress, X_t is the tensile strength of the matrix, and X_{22} and X_{12} are transverse and shear strength, respectively, of the fiber-reinforced regions. The strength properties X_{22} and X_{12} in function of the fiber volume fraction are computed using the Chamis formulae. Interface debonding is evaluated based on Ye's criterion [58]:

$$f_{int} = \sqrt{(\frac{< \sigma_{nn} >}{X_{nn}})^2 + (\frac{\sigma_{nt}}{X_{nt}})^2} \geq 1$$

where $< . >$ is the MacAuley bracket defined as $< x >= \frac{1}{2}(x + |x|)$, σ_{nn} and σ_{tn} are the normal and tangential stress component, respectively, at the interface and X_{nn} and X_{tn} are the corresponding mode-1 and mode-2 interfacial strengths (see Table 4). A 97-percentile of each damage initiation indicator (as defined in [50]) will further be used to compare the local damage initiation indicator distribution between the different models.

Stiffness	carbon fiber	epoxy matrix	strength	carbon fiber	epoxy matrix	interface
$E_{11}(GPa)$	231	3.45	$X_{11,t}(MPa)$	3500	70	-
$E_{22}(GPa)$	15	-	$X_{11,c}(MPa)$	3000	130	-
$E_{33}(GPa)$	15	-	$X_{12}(MPa)$	-	57	-
v_{12}	0.20	0.35	$\epsilon^f_{11,t}(\%)$	1.51	4.5	-
v_{13}	0.20	-	$\epsilon^f_{11,c}(\%)$	1.30	8	-
v_{23}	0.20	-	$\gamma^f_{12}(\%)$	-	5	-
$G_{12}(GPa)$	15	1.28	$X_{nn}(MPa)$	-	-	80
$G_{13}(GPa)$	7	-	$X_{nt}(MPa)$	-	-	100
$G_{23}(GPa)$	7	-				

Table 4: The stiffness and strength properties of carbon fiber (type AS4 [59]) and epoxy matrix (type 5260 [59]), and the strength properties of the interface between the fiber-reinforced regions and the matrix [60].

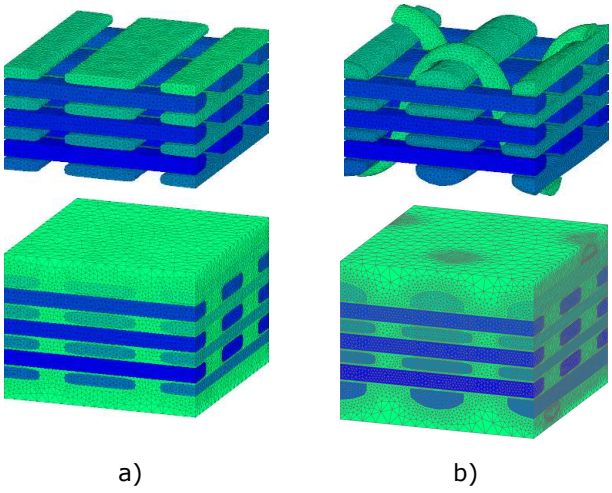

Figure 14: Generated mesh models for: (a) the non 3D woven model, (b) the 3D woven model.

5.1. Models

The effect of 3D weaving, cross-section variations in the surface weft yarns and cross-section variations in the binder yarn on the overall stiffness of the composite of the composite and on the damage initiation is evaluated by the following three cases:

Case 1, the effect of 3D weaving is investigated by comparing the results

of a 3D woven model with an equivalent non 3D-woven composite model. The 3D woven model is obtained using the generation procedures and parameters presented in Table 2 and Table 3 respectively. The equivalent non 3D woven model is considered in this work as the initial configuration of the 3D woven model but without the binder yarn and with the cross-sections of the surface weft yarns taken equal to the cross-sections of the inner weft yarns. The meshed models for both configurations are illustrated in Fig. 14.

Case 2, the effect of cross-section variations in the surface weft yarn is investigated by generating 3D woven models whereby the parameter s_2 in generation step 4 is varied (see Table 2). Surface weft yarn geometries for the different parameters s_2 are similar to the illustrations presented in Fig. 10.

Case 3, the effect of cross-section variations in the binder yarn is investigated by generating 3D woven models in which the parameter s_3 in generation step 6 (see Table 2) is varied. Binder yarn geometries for the different values of the parameter s_3 are similar to the illustrations presented in Fig. 12.

5.2. Results

5.2.1. Effect of 3D weaving (case 1)

The normalized stiffness components of the 3D woven model are presented in Table 5. When considering the 3D weaving, the stiffness in the warp direction is slightly increased (2%) while the stiffness in the weft- and bias-direction are increased in larger proportion (12% and 14% respectively). Note that the stiffness in the bias-direction is approximately 10 times lower than the stiffness in the warp and weft direction. The stiffness components fall in the range of experimental observations [10] which has shown to be between 0.80 and 1.20. It therefore remains ambiguous whether 3D weaving increases or decrease the stiffness.

The damage initiation indicator distributions in the 3D woven model for

warp-, weft- and bias-loading are summarized by their 97-percentile in Table 6 for different loading modes. The 97-percentile of the local damage initiation indicators in the fiber-reinforced regions and matrix are increased, which indicates that damage initiation will occur earlier in a 3D woven composite than in an equivalent composite. Transverse damage in the surface weft yarn, transverse damage in the binder yarn, and shear damage in the surface weft and binder yarn are the main damage initiation mechanisms taking place for warp-, weft- and bias-loading respectively. The warp- and bias- directions experience higher damage initiation indicators more damage with respect the weft-direction, making them the most critical directions to be looked after in the design of the 3D woven composites. The potential regions in which damage initation may occur (see Fig. 15) correlate hereby with the most distorted fiber-reinforced regions (see Fig. 13) which are located near the binder locations.

The damage initiation characteristics from the simulations results substantiate with experimental observation as follows. Early damage initiation and stress concentrations near binder locations, as observed in the simulation results, have also been observed experimentally in earlier works [5, 7, 16]. For warp-loading, the very small damage appeared experimentally first near the middle section of the Z-crown crossover with the adjacent surface weft yarns, which is then followed by transverse damage in the weft yarns under increasing load [5]. For weft-loading, the damage is initiated in the form of transverse damage in the warp and binder yarns [5]. For the bias direction, the damage starts at the Z-crowns [5]. Similar trends can be observed for damage initiation in the simulation results presented in Fig. 15.

E_{norm}^{warp}	1.02	E_{norm}^{weft}	1.12	E_{norm}^{shear}	1.14

Table 5: The normalised stiffness components of the 3D woven model.

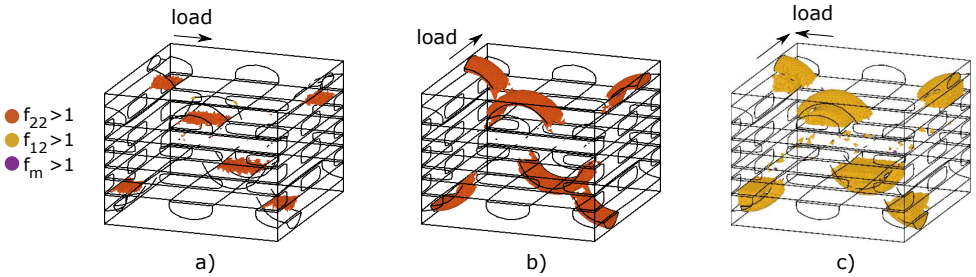

Figure 15: An illustration of the potential local damage initiated regions in the 3D woven model, with an indication of the main local damage initiation mechanisms, for different loading directions: (a) warp-direction, (b) weft-direction and (c) shear-direction.

		binder			inner weft		surface weft			matrix
		$f_{22}^{97\%}$	$f_{12}^{97\%}$	$f_{int}^{97\%}$	$f_{22}^{97\%}$	$f_{12}^{97\%}$	$f_{22}^{97\%}$	$f_{12}^{97\%}$	$f_{int}^{97\%}$	$f_{m}^{97\%}$
warp-load	equivalent	-	-	-	0.52	0.01	0.51	0.01	0.30	0.36
	3D woven	0.16	0.22	0.41	0.71	0.05	0.80	0.11	0.34	0.43
weft-load	equivalent	-	-	-	0.13	0.01	0.12	0.01	0.08	0.35
	3D woven	1.82	0.18	0.45	0.16	0.02	0.41	0.21	0.17	0.39
shear-load	equivalent	-	-	-	0.04	0.75	0.03	0.69	0.26	0.33
	3D woven	0.25	1.77	0.45	0.08	0.97	0.10	1.55	0.29	0.41

Table 6: The 97-percentile of the local damage initiation indicators in the binder, the inner and surface weft yarns, and the matrix.

5.2.2. Effect of cross-section variations in the surface weft yarns (case 2)

The effect of cross-sections variations in the surface weft yarns is investigated (Fig. 16a) on the stiffness of the 3D woven model and on transverse and shear damage initiation indicators in the surface weft yarns for warp- and bias-loading (as being the most critical cases, see Table 6) respectively. The stiffness components of the 3D woven models are normalised by the stiffness of the 3D woven model in which the surface weft yarns are fully straight (setup corresponding to $s_2 = 100$). The considered damage initiation indicators are presented in the fiber-bundles by their average. An increased average would then indicate an increased probability of early damage initation in regions with a damage initiation

indicator lower than the maximum damage initiation indicator as well as a faster propagation of cracks after their initiation at the most critical location[55]. Realistic cross-section variations in a fiber-bundle correspond then to a value for s_2 lying between 20 and 100, as these values corresponds to experimentally observed maximum in-plane fiber misalignment that lie in between 0° and 10° [10].

It can be seen (in Fig. 16a) that a small s_2-value (corresponding to a large maximum in-plane fiber misalignment) can result in lower stiffness components and in a lower average of the transverse and shear damage initiation indicators than a large s_2-value (corresponding to a small maximum in-plane fiber misalignment). 3D woven models assuming straight weft yarn (as adopted in [61–64]) may then overestimate the risk for damage initiation.

5.2.3. Effect cross-section variations in binder yarn (case 3)

The effect of cross-section variations in the binder yarn is now investigated (Fig. 16b) on the stiffness of the 3D woven model, and on the transverse and shear damage initiation indicators in the binder yarn for weft- and shear-loading respectively (as being the main critical damage indicators in the binder yarn, see Table 6). The thickness of the cross-section in the top segment of the binder yarn, normalised by the thickness of the initial cross-section of the binder yarn, and the average of the fiber volume fraction distribution in the binder yarns are presented as well. The stiffness components of the 3D woven models are further normalised by the stiffness of the 3D woven model with constant cross-sections for the binder yarn ($s_3 = 0$) and the average for the considered damage initiation indicators is considered. Realistic values of s_3 would lie in the range from 4 and 12 (dependent on binder content and tensioning), which corresponds to experimentally observed values of the normalised thickness that typically lies in the range $0.30 - 0.70$ (as can be deduced from experimental figures presented in [7, 20, 21, 30, 34]).

It can be seen (in Fig. 16b) that a small s_3 value (corresponding to small

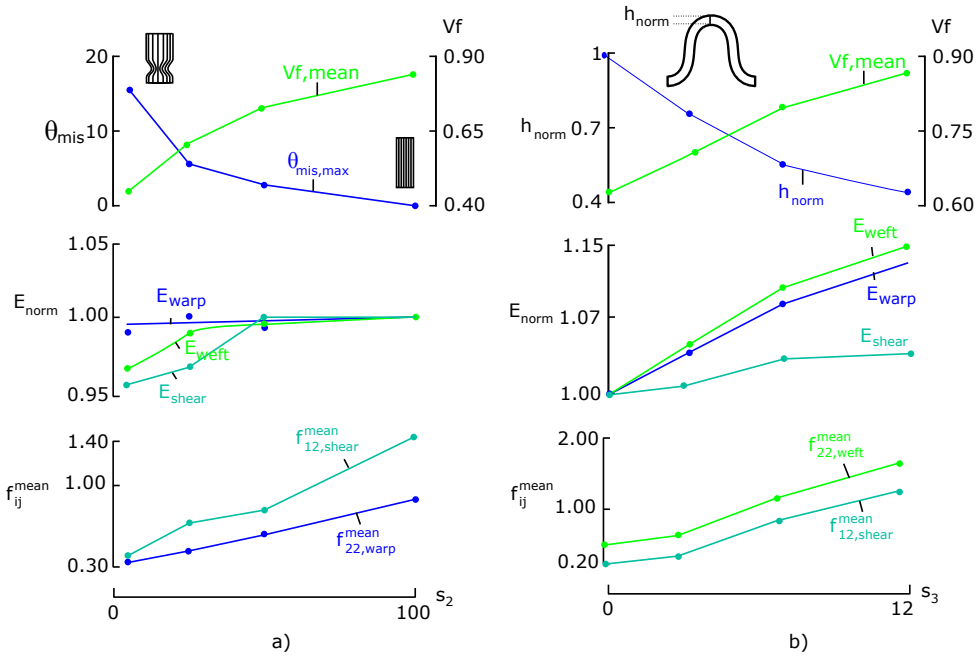

Figure 16: Graphs showing the effect of cross-section variations in surface weft yarn and binder yarn: (a) the maximum in-plane fiber misalignment and the mean of the fiber volume fraction in the surface weft yarns, the stiffness components, and the mean of transverse damage initiation indicators (for warp-loading) and shear damage initiation indicator (for shear-loading) in the surface weft yarns are presented for varying parameters s_2 - (b) the normalised thickness of the cross-section in the top segment of the binder yarn and the mean of the fiber volume fraction in the binder yarn, the stiffness components, and the mean of the transverse damage initiation indicators (for weft-loading) and the shear damage initiation indicators (for warp-loading) are presented for varying parameters s_3.

binder yarn cross-section variations), results in a lower stiffness and a lower average value of the local damage initiation indicators than a large s_3 value (corresponding to large binder yarn cross-section variations). 3D woven models with a constant assumed cross-section for the binder yarn and with a matrix that fully embeds the binder yarn (as adopted in [61–64]) would then underestimate the stiffness and the average value of the local damage initiation indicators with a level of underestimation dependent on the binder content. The increase in stiffness of 3D woven models embedding a binder yarn with large cross-section

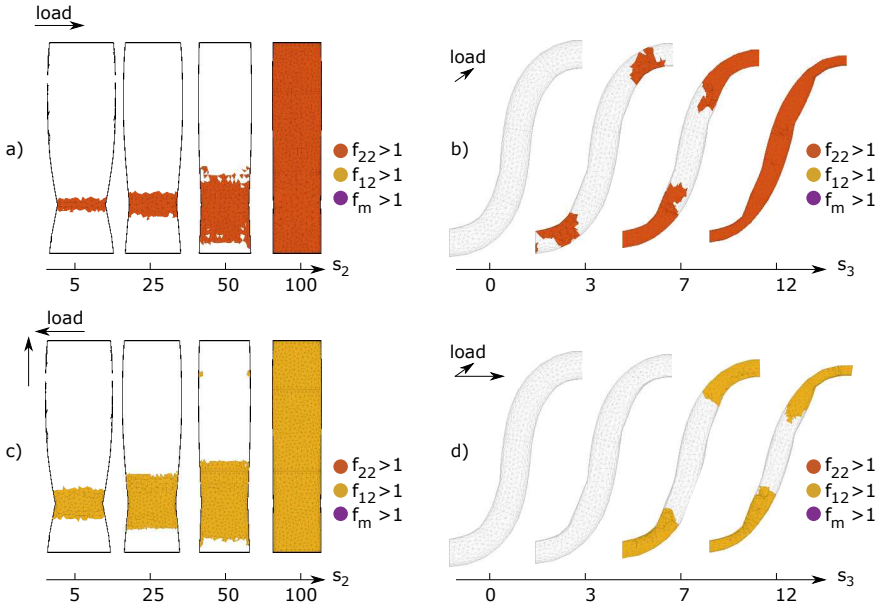

Figure 17: The corresponding potential local damage initiated regions in the surface or binder yarn for the different cross-section variations configurations analysed in Section 4: (a) transverse damage in surface weft yarn for warp-loading, (b) transverse damage in binder yarn for weft-loading, (c) shear damage in surface weft yarn for shear-loading, (d) shear damage in binder yarn for shear-loading

variations is related to the fact that the matrix is defined around the binder yarn, which can easily be resolved by considering a matrix that only surrounds the in-plane fiber-reinforced regions (as done in [51]).

6. Discussion

6.1. Comparing geometrical modelling approaches

The centerline and cross-sections of fiber-bundles in 3D woven models can be shaped using analytical, digital element and geometrical-based modelling approaches as presented in this work.

1. Analytical modelling approaches shape the fiber-bundles in 3D woven composites manually by means of functional representations. Different func-

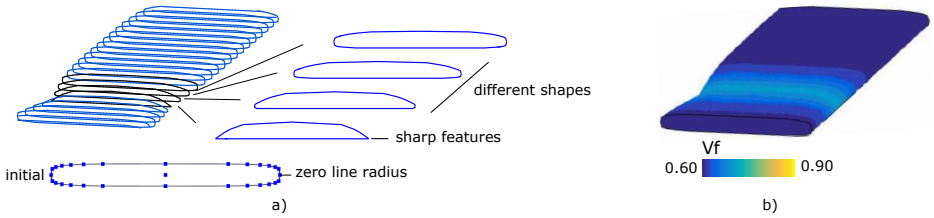

Figure 18: A reflection on the geometrical model generation approach: (a) smooth cross-section shape variations caused by binder insertion in the surface weft can be generated by adopting a zero line-radius in the boundary-lines configuration, (b) the constant assumed fiber volume fraction V_f in cross-section may not correctly the V_f-distribution in a cross-section of the surface weft yarns for small binder content.

tional representations need to be adopted each time the shape of geometrical features changes, as for example due to binder content and binder tensioning, making analytical models less general to include the main geometrical details for a wide range of binder parameters, but a full control over the shape of geometrical features is present.

2. Digital element approaches shape the fiber-bundles in 3D woven composites by considering an inner-line configurations for each fiber-bundle. The fiber-bundles are positioned initially in a loose-state configuration, and are then gradually shaped by a binder yarn tensioning and transverse compaction during finite element simulations. The shape of fiber-bundles which are conforming with each other and correlated with a binder yarn tensioning and transverse compaction loading can hereby be automatically generated. It should be noted that this approach is computationally expensive and requires a line-radius which may cause a loss of accuracy on the extracted cross-section shapes during an offset post-processing procedure.
3. The geometrical-based approach as presented in this work shape the fiber-bundles by means of a boundary-line and inner-line configuration (for weft and binder yarn respectively), based on geometrical operations. The boundary-line configuration allows modelling small changes in the cross-

sections shapes in fiber-bundle with straight centerlines, as illustrated in Fig. 7a). Conversely, the inner-line configuration allows automatically accounting for cross-section variations in fiber-bundle due to different stages of binder yarn tensioning (similar to the digital element approach). An essential difference lies in the lower cost of the presented approach. The geometrical-based framework can generate unit-cell models in the order of minute as it does not require expensive finite element simulations. It should be emphasized though that the predictive nature of the approach is limited as no mechanics is involved. The combination of an inner-line configuration and a geometrical-based framework to shape cross-section variations in fiber-bundles for transverse compaction loading should still be investigated, but the principles explained here should allow such an extension.

The selection of a modelling approach adopted for the generation of 3D woven models can then depend on a desired generality, simplicity, computational time, and control over the obtained shape of the geometrical features, etc.

6.2. Role of local fiber volume fraction

Local fiber volume fractions have already been shown in fiber-reinforced composites to act as stress concentration and damage initiation regions [50, 51, 55, 65, 66]. A similar trend can also be observed in this work, by comparing the contour plots of the regions of stress concentrations in the surface weft and binder yarns illustrated in Fig. 17 with the corresponding fiber volume fraction distributions presented in Fig. 10 and Fig. 12 for the surface weft and binder yarn respectively. The location of the stress concentration regions are observed to be correlated with the locations of increased fiber-volume fraction. Such a positive correlation further indicates the importance to include the local fiber volume fraction correctly in the models. Still, a uniform fiber volume fraction in each cross-section of the fiber-bundles is assumed in this work, but may be unrealistic in 3D woven models with a smaller binder content or tensioning (see Fig. 7b) whereby the distortions should only take place near the borders ([53]).

A locally distorted zone in the surface weft yarns should then be adopted to account more properly for fiber volume fraction variations. Local fiber-reinforced distorted zone models similar to [50, 51] for z-pinned and stitched laminates can therefore be adopted.

6.3. Effect of simplified geometrical features

Centerline deflections of the in-plane fiber-bundles and flattening of the binder-yarn cross-section, which may arise during excessive transverse compaction and binder yarn tensioning, are not included in the models. This may have the following effects on the mechanical behaviour:

1. Not including centerline deflections of in-plane fiber-bundles can result in an overestimation of in-plane stiffness and an underestimation of local stress levels in neighbouring fiber-bundles of the considered deflected fiber-bundles at their deflection points.
2. Not including flattened cross-sections of the binder yarn enlarges the amount of matrix that surrounds fully the binder yarn, and as such can results in an underestimation of the stiffness while the stress concentrations in the top segment of the binder yarn may be underestimated.

The quantitative effect of these assumptions should be mechanically investigated and are assumed in this work to fall in the experimental range.

7. Conclusion

An approach was presented to generate automatically mesoscopic unit-cell models of 3D orthogonal woven non-crimp fabric composites which include cross-section variations in the surface weft and the binder yarns. A boundary-line and inner-line configuration are considered for the weft and binder yarns respectively to account for the cross-section shapes variations. Geometrical operations are applied to shapes the discretised lines. Shapes of the binder and surface weft yarn corresponding to different binder contents and tensioning can be obtained automatically, resulting in an efficient production of simulation-ready RVEs.

Mechanical simulations have further shown the importance of including the stitching yarn, out-of-plane undulations and local fiber-reinforcement distortions in models for stiffness and damage initiation predictions. The approach can be adopted for both the construction of physical models and as tool to investigate the effect of binder parameters on the overall mechanical behaviour.

In future works, firstly, the possibility of the approach to generate unit-cell models for different 3D woven configurations (angle-interlock or layer to layer) should be assessed, including more explicitly the potential effects of transverse compaction on the binder yarn centerline and cross-section variations shapes as well as centerline deflections of the in-plane fiber-bundles as an output of the procedure. Secondly, unit-cell models for the different binder configuration should be both qualitatively and quantitatively compared in terms of geometries and mechanical behaviour. Finally, the finite element simulations should be extended by more elaborate damage initiation models (Puck [67], Hashin [68]) and by damage constitutive laws for strength modelling purposes, as well as by out-of-plane loading conditions to assess the out-of-plane behaviour of these RVEs.

Acknowledgements

The first author acknowledges the support of IWT under Grant No. IWT-SB-678.

8. References

[1] V. A. Guénon, T.-W. Chou, J. W. Gillespie, Toughness properties of a three-dimensional carbon-epoxy composite, Journal of materials science 24 (11) (1989) 4168–4175.

[2] Y. Tanzawa, N. Watanabe, T. Ishikawa, Interlaminar fracture toughness of 3-d orthogonal interlocked fabric composites, Composites Science and Technology 59 (8) (1999) 1261–1270.

[3] Y. Tanzawa, N. Watanabe, T. Ishikawa, Fem simulation of a modified dcb test for 3-d orthogonal interlocked fabric composites, Composites Science and Technology 61 (8) (2001) 1097–1107.

[4] S. Lomov, A. Bogdanovich, D. Ivanov, D. Mungalov, M. Karahan, I. Verpoest, A comparative study of tensile properties of non-crimp 3d orthogonal weave and multi-layer plain weave e-glass composites. part 1: Materials, methods and principal results, Composites part a: applied science and manufacturing 40 (8) (2009) 1134–1143.

[5] D. Ivanov, S. Lomov, A. Bogdanovich, M. Karahan, I. Verpoest, A comparative study of tensile properties of non-crimp 3d orthogonal weave and multi-layer plain weave e-glass composites. part 2: Comprehensive experimental results, Composites part a: applied science and manufacturing 40 (8) (2009) 1144–1157.

[6] A. E. Bogdanovich, Advancements in manufacturing and applications of 3d woven preforms and composites, in: 16th international conference on composite materials, Citeseer, 2006, pp. 1–10.

[7] S. Dai, P. Cunningham, S. Marshall, C. Silva, Influence of fibre architecture on the tensile, compressive and flexural behaviour of 3d woven composites, Composites Part A: Applied Science and Manufacturing 69 (2015) 195–207.

[8] K. Leong, B. Lee, I. Herszberg, M. Bannister, The effect of binder path on the tensile properties and failure of multilayer woven cfrp composites, Composites Science and Technology 60 (1) (2000) 149–156.

[9] P. Callus, A. Mouritz, M. K. Bannister, K. Leong, Tensile properties and failure mechanisms of 3d woven grp composites, Composites Part A: Applied Science and Manufacturing 30 (11) (1999) 1277–1287.

[10] A. Mouritz, B. Cox, A mechanistic interpretation of the comparative in-plane mechanical properties of 3d woven, stitched and pinned composites, Composites Part A: Applied Science and Manufacturing 41 (6) (2010) 709–728.

[11] D. Fishpool, A. Rezai, D. Baker, S. Ogin, P. Smith, Interlaminar toughness characterisation of 3d woven carbon fibre composites, Plastics, Rubber and Composites 42 (3) (2013) 108–114.

[12] G. Stegschuster, K. Pingkarawat, B. Wendland, A. Mouritz, Experimental determination of the mode i delamination fracture and fatigue properties of thin 3d woven composites, Composites Part A: Applied Science and Manufacturing 84 (2016) 308–315.

[13] B. N. Cox, M. S. Dadkhah, W. Morris, On the tensile failure of 3d woven composites, Composites Part A: Applied Science and Manufacturing 27 (6) (1996) 447–458.

[14] W.-S. Kuo, T.-H. Ko, Compressive damage in 3-axis orthogonal fabric composites, Composites Part A: Applied Science and Manufacturing 31 (10) (2000) 1091–1105.

[15] M. Bannister, I. Herszberg, A. Nicolaidis, F. Coman, K. Leong, The manufacture of glass/epoxy composites with multilayer woven architectures, Composites Part A: Applied Science and Manufacturing 29 (3) (1998) 293–300.

[16] A. Bogdanovich, M. Karahan, S. Lomov, I. Verpoest, Quasi-static tensile behavior and damage of carbon/epoxy composite reinforced with 3d non-crimp orthogonal woven fabric, Mechanics of Materials 62 (2013) 14–31.

[17] S. Lomov, D. Ivanov, I. Verpoest, M. Zako, T. Kurashiki, H. Nakai, S. Hirosawa, Meso-fe modelling of textile composites: Road map, data flow and algorithms, Composites Science and Technology 67 (9) (2007) 1870–1891.

[18] M. Ansar, W. Xinwei, Z. Chouwei, Modeling strategies of 3d woven composites: a review, Composite structures 93 (8) (2011) 1947–1963.

[19] B. Piezel, B. Mercatoris, W. Trabelsi, L. Laiarinandrasana, A. Thionnet, T. J. Massart, Bending effect on the risk for delamination at the reinforcement/matrix interface of 3d woven fabric composite using a shell-like rve, Composite structures 94 (8) (2012) 2343–2357.

[20] F. Desplentere, S. Lomov, D. Woerdeman, I. Verpoest, M. Wevers, A. Bogdanovich, Micro-ct characterization of variability in 3d textile architecture, Composites Science and Technology 65 (13) (2005) 1920–1930.

[21] X. Zeng, L. Brown, A. Endruweit, M. Matveev, A. Long, Geometrical modelling of 3d woven reinforcements for polymer composites: Prediction of fabric permeability and composite mechanical properties, Composites Part A: Applied Science and Manufacturing 56 (2014) 150–160.

[22] M. Karahan, S. Lomov, A. Bogdanovich, D. Mungalov, I. Verpoest, Internal geometry evaluation of non-crimp 3d orthogonal woven carbon fabric composite, Composites Part A: Applied Science and Manufacturing 41 (9) (2010) 1301–1311.

[23] A. Labanieh, Y. Liu, D. Vasiukov, D. Soulat, S. Panier, Influence of off-axis in-plane yarns on the mechanical properties of 3d composites, Composites Part A: Applied Science and Manufacturing 98 (2017) 45–57.

[24] Y. Mahadik, K. R. Brown, S. Hallett, Characterisation of 3d woven composite internal architecture and effect of compaction, Composites Part A: Applied Science and Manufacturing 41 (7) (2010) 872–880.

[25] N. Naouar, E. Vidal-Salle, J. Schneider, E. Maire, P. Boisse, 3d composite reinforcement meso fe analyses based on x-ray computed tomography, Composite Structures 132 (2015) 1094–1104.

[26] Y. Liu, I. Straumit, D. Vasiukov, S. Lomov, S. Panier, Prediction of linear and non-linear behavior of 3d woven composite using mesoscopic voxel models reconstructed from x-ray micro-tomography, Composite Structures 179 (2017) 568–579.

[27] L. Tong, A. Mouritz, M. Bannister, 3D fibre reinforced polymer composites, Elsevier, 2002.

[28] F. Coman, L. Herszberg, M. Bannister, S. John, Design and analysis of 3d woven preforms for composite structures, Science and Engineering of Composite Materials 5 (2) (1996) 83–96.

[29] L. Lee, S. Rudov-Clark, A. Mouritz, M. Bannister, I. Herszberg, Effect of weaving damage on the tensile properties of three-dimensional woven composites, Composite Structures 57 (1-4) (2002) 405–413.

[30] N. Isart, J. Mayugo, N. Blanco, L. Ripoll, A. Solà, M. Soler, Geometric model for 3d through-thickness orthogonal interlock composites, Composite Structures 119 (2015) 787–798.

[31] H. Lin, X. Zeng, M. Sherburn, A. Long, M. Clifford, Automated geometric modelling of textile structures, Textile Research Journal 82 (16) (2012) 1689–1702.

[32] S. Lomov, G. Huysmans, Y. Luo, R. Parnas, A. Prodromou, I. Verpoest, F. Phelan, Textile composites: modelling strategies, Composites Part A: applied science and manufacturing 32 (10) (2001) 1379–1394.

[33] T. Sagar, P. Potluri, J. Hearle, et al., Mesoscale modelling of interlaced fibre assemblies using energy method, Computational Materials Science 28 (1) (2003) 49–62.

[34] S. Lomov, G. Perie, D. Ivanov, I. Verpoest, D. Marsal, Modeling three-dimensional fabrics and three-dimensional reinforced composites: challenges and solutions, Textile Research Journal 81 (1) (2011) 28–41.

[35] B. El Said, S. Green, S. Hallett, Kinematic modelling of 3d woven fabric deformation for structural scale features, Composites Part A: Applied Science and Manufacturing 57 (2014) 95–107.

[36] S. Green, A. Long, B. El Said, S. Hallett, Numerical modelling of 3d woven preform deformations, Composite Structures 108 (2014) 747–756.

[37] S. Green, M. Matveev, A. Long, D. Ivanov, S. Hallett, Mechanical modelling of 3d woven composites considering realistic unit cell geometry, Composite Structures 118 (2014) 284–293.

[38] L. Huang, Y. Wang, Y. Miao, D. Swenson, Y. Ma, C. Yen, Dynamic relaxation approach with periodic boundary conditions in determining the 3-d woven textile micro-geometry, Composite Structures 106 (2013) 417–425.

[39] A. Thompson, B. El Said, D. Ivanov, J. Belnoue, S. Hallett, High fidelity modelling of the compression behaviour of 2d woven fabrics, International Journal of Solids and Structures.

[40] Z. Yousaf, P. Potluri, P. Withers, D. Mollenhauer, E. Zhou, S. Duning, Digital element simulation of aligned tows during compaction validated by computed tomography (ct), International Journal of Solids and Structures.

[41] Y. Wang, X. Sun, Digital-element simulation of textile processes, Composites science and technology 61 (2) (2001) 311–319.

[42] Y. Miao, E. Zhou, Y. Wang, B. Cheeseman, Mechanics of textile composites: Micro-geometry, Composites Science and Technology 68 (7-8) (2008) 1671–1678.

[43] D. Durville, A finite element approach of the behaviour of woven materials at microscopic scale, in: Mechanics of microstructured solids, Springer, 2009, pp. 39–46.

[44] D. Durville, Simulation of the mechanical behaviour of woven fabrics at the scale of fibers, International journal of material forming 3 (2) (2010) 1241–1251.

[45] Y. Mahadik, S. Hallett, Finite element modelling of tow geometry in 3d woven fabrics, Composites Part A: Applied Science and Manufacturing 41 (9) (2010) 1192–1200.

[46] F. Stig, S. Hallström, Spatial modelling of 3d-woven textiles, Composite structures 94 (5) (2012) 1495–1502.

[47] F. Stig, S. Hallström, A modelling framework for composites containing 3d reinforcement, Composite Structures 94 (9) (2012) 2895–2901.

[48] B. Sonon, B. Francois, T. J. Massart, A unified level set based methodology for fast generation of complex microstructural multi-phase rves, Computer methods in applied mechanics and engineering 223 (2012) 103–122.

[49] B. Wintiba, B. Sonon, K. Kamel, T. J. Massart, An automated procedure for the generation and conformal discretization of 3d woven composites rves, Composite Structures 180 (2017) 955–971.

[50] G. Pierreux, L. Wu, D. Van Hemelrijck, T. J. Massart, Evaluation of microdamage initiation in z-pinned laminates by means of automated rve computations, Composite Structures 206 (2018) 104–115.

[51] G. Pierreux, Automated unit-cell model generation for micro-mechanical simulations of 3d reinforced composites, Ph.D. thesis, Université libre de Bruxelles and Vrije Universiteit Brussel, Brussels (2018).

[52] B. Cox, M. Dadkhah, W. Morris, J. Flintoff, Failure mechanisms of 3d woven composites in tension, compression, and bending, Acta metallurgica et materialia 42 (12) (1994) 3967–3984.

[53] Y. Liu, Multi-scale damage modelling of 3d textile reinforced composites including microstructural variability generation and meso-scale reconstruction, Ph.D. thesis, Lille 1 (2017).

[54] C. Chamis, Mechanics of composite materials: past, present, and future, Journal of Composites, Technology and Research 11 (1) (1989) 3–14.

[55] A. Yudhanto, N. Watanabe, Y. Iwahori, H. Hoshi, Effect of stitch density on tensile properties and damage mechanisms of stitched carbon/epoxy composites, Composites Part B: Engineering 46 (2013) 151–165.

[56] A. Yudhanto, G. Lubineau, I. Ventura, N. Watanabe, Y. Iwahori, H. Hoshi, Damage characteristics in 3d stitched composites with various stitch parameters under in-plane tension, Composites Part A: Applied Science and Manufacturing 71 (2015) 17–31.

[57] F. Edgren, C. Soutis, L. Asp, Damage tolerance analysis of ncf composite sandwich panels, Composites Science and Technology 68 (13) (2008) 2635–2645.

[58] L. Ye, Role of matrix resin in delamination onset and growth in composite laminates, Composites science and technology 33 (4) (1988) 257–277.

[59] A. Kaddour, M. Hinton, P. Smith, S. Li, Mechanical properties and details of composite laminates for the test cases used in the third world-wide failure exercise, Journal of Composite Materials 47 (20-21) (2013) 2427–2442.

[60] A. Turon, P. P. Camanho, J. Costa, C. Dávila, A damage model for the simulation of delamination in advanced composites under variable-mode loading, Mechanics of Materials 38 (11) (2006) 1072–1089.

[61] P. Biragoni, S. Hallett, Finite element modelling of 3d woven composites for stiffness prediction, in: 17th International Conference on Composite Materials (ICCM-17), 2009.

[62] X. Wang, X. Wang, G. Zhou, C. Zhou, Multi-scale analyses of 3d woven composite based on periodicity boundary conditions, Journal of Composite Materials 41 (14) (2007) 1773–1788.

[63] C. Lee, S. Chung, H. Shin, S. Kim, Virtual material characterization of 3d orthogonal woven composite materials by large-scale computing, Journal of composite materials 39 (10) (2005) 851–863.

[64] J. Crookston, S. Kari, N. Warrior, I. Jones, A. Long, 3d textile composite mechanical properties prediction using automated fea of the unit cell, in: Proc. of the 16th Int. Conf. on Composite Materials, 2007, pp. 1–7.

[65] J. Faes, A. Rezaei, W. Van Paepegem, J. Degrieck, Accuracy of 2d fe models for prediction of crack initiation in nested textile composites with inhomogeneous intra-yarn fiber volume fractions, Composite Structures 140 (2016) 11–20.

[66] R. Sevenois, D. Garoz, F. Gilabert, S. Spronk, S. Fonteyn, M. Heyndrickx, L. Pyl, D. Van Hemelrijck, J. Degrieck, W. Van Paepegem, Avoiding interpenetrations and the importance of nesting in analytic geometry construction for representative unit cells of woven composite laminates, Composites Science and Technology 136 (2016) 119–132.

[67] A. Puck, H. Schürmann, Failure analysis of frp laminates by means of physically based phenomenological models, in: Failure Criteria in Fibre-Reinforced-Polymer Composites, Elsevier, 2004, pp. 832–876.

[68] Z. Hashin, Failure criteria for unidirectional fiber composites, Journal of applied mechanics 47 (2) (1980) 329–334.